Silicon photonics plasma-modulators with advanced transmission line design

Florian Merget,[1,*] Saeed Sharif Azadeh,[1] Juliana Mueller,[1] Bin Shen,[1] Maziar P. Nezhad,[1] Johannes Hauck,[1] and Jeremy Witzens[1]

[1]*The Integrated Photonics Laboratory (IPH) of RWTH-Aachen University, Sommerfeldstr. 24, 52074 Aachen, Germany*

[*]*fmerget@iph.rwth-aachen.de*

Abstract: We have investigated two novel concepts for the design of transmission lines in travelling wave Mach-Zehnder interferometer based Silicon Photonics depletion modulators overcoming the analog bandwidth limitations arising from cross-talk between signal lines in push-pull modulators and reducing the linear losses of the transmission lines. We experimentally validate the concepts and demonstrate an E/O −3 dBe bandwidth of 16 GHz with a 4V drive voltage (in dual drive configuration) and 8.8 dB on-chip insertion losses. Significant bandwidth improvements result from suppression of cross-talk. An additional bandwidth enhancement of ~11% results from a reduction of resistive transmission line losses. Frequency dependent loss models for loaded transmission lines and E/O bandwidth modeling are fully verified.

©2013 Optical Society of America

OCIS codes: (230.7020) Travelling-wave devices; (130.4110) Modulators; (250.4110) Modulators; (250.7360) Waveguide modulators; (230.3120) Integrated optics devices; (230.2090) Electro-optical devices.

References and links

1. A. Liu, R. Jones, L. Liao, D. Samara-Rubio, D. Rubin, O. Cohen, R. Nicolaescu, and M. Paniccia, "A high-speed silicon optical modulator based on a metal-oxide-semiconductor capacitor," Nature **427**(6975), 615–618 (2004).
2. K. Preston, S. Manipatruni, A. Gondarenko, C. B. Poitras, and M. Lipson, "Deposited silicon high-speed integrated electro-optic modulator," Opt. Express **17**(7), 5118–5124 (2009).
3. G. T. Reed, G. Mashanovich, F. Y. Gardes, and D. J. Thomson, "Silicon optical modulators," Nature **4**, 518–526 (2010).
4. D. Kucharski, D. Guckenberg, G. Masini, S. Abdalla, J. Witzens, and S. Sahni, "10Gb/s 15mW Optical Receiver with Integrated Germanium Photodetector and Hybrid Inductor Peaking in 0.13µm SOI CMOS Technology," Proc. 2010 IEEE Intern. Sol.-State Circ. Conf. (ISSCC), 360–361 (2010).
5. J. K. Doylend, A. P. Knights, B. J. Luff, R. Shafiiha, M. Asghari, and R. M. Gwilliam, "Modifying functionality of variable optical attenuator to signal monitoring through defect engineering," Electron. Lett. **46**(3), 234–236 (2010).
6. G. Masini, G. Capellini, J. Witzens, and C. Gunn, "High-speed, monolithic CMOS receivers at 1550 nm with Ge on Si waveguide photodetectors," Proc. Lasers and Electro-Optics Soc. (LEOS), 848–849 (2007).
7. L. Vivien, J. Osmond, J.-M. Fédéli, D. Marris-Morini, P. Crozat, J.-F. Damlencourt, E. Cassan, Y. Lecunff, and S. Laval, "42 GHz p.i.n Germanium photodetector integrated in a silicon-on-insulator waveguide," Opt. Express **17**(8), 6252–6257 (2009).
8. W. M. J. Green, M. J. Rooks, L. Sekaric, and Y. A. Vlasov, "Ultra-compact, low RF power, 10 Gb/s silicon Mach-Zehnder modulator," Opt. Express **15**(25), 17106–17113 (2007).
9. G.-R. Zhou, M. W. Geis, S. J. Spector, F. Gan, M. E. Grein, R. T. Schulein, J. S. Orcutt, J. U. Yoon, D. M. Lennon, T. M. Lyszczarz, E. P. Ippen, and F. X. Käertner, "Effect of carrier lifetime on forward-biased silicon Mach-Zehnder modulators," Opt. Express **16**(8), 5218–5226 (2008).
10. J. Thomson, F. Y. Gardens, J.-M. Fédéli, S. Zlatanovic, Y. Hu, B. P. P. Kuo, E. Myslivets, N. Alic, S. Radic, G. Z. Mashanovich, and G. Reed, "50-Gb/s silicon optical modulator," IEEE Photon. Technol. Lett. **24**(4), 234–236 (2012).
11. T. Y. Liow, K. Ang, Q. Fang, J. Song, Y. Xiong, M. Yu, G. Lo, and D. Kwong, "Silicon modulators and germanium photodetectors on SOI: monolithic integration, compatibility, and performance optimization," IEEE J. Sel. Top. Quantum Electron. **16**(1), 307–315 (2010).
12. T. Baehr-Jones, R. Ding, Y. Liu, A. Ayazi, T. Pinguet, N. C. Harris, M. Streshinsky, P. Lee, Y. Zhang, A. E. Lim, T. Y. Liow, S. H. G. Teo, G. Q. Lo, and M. Hochberg, "Ultralow drive voltage silicon traveling-wave modulator," Opt. Express **20**(11), 12014–12020 (2012).

#193401 - $15.00 USD Received 5 Jul 2013; revised 2 Aug 2013; accepted 3 Aug 2013; published 13 Aug 2013

13. H. Yu, M. Pantouvaki, J. Van Campenhout, D. Korn, K. Komorowska, P. Dumon, Y. L. Li, P. Verheyen, P. Absil, L. Alloatti, D. Hillerkuss, J. Leuthold, R. Baets, and W. Bogaerts, “Performance tradeoff between lateral and interdigitated doping patterns for high speed carrier-depletion based silicon modulators,” Opt. Express **20**(12), 12926–12938 (2012).
14. R. Ding, T. Baehr-Jones, Y. Liu, R. Bojko, J. Witzens, S. Huang, J. Luo, S. Benight, P. Sullivan, J. M. Fedeli, M. Fournier, L. Dalton, A. Jen, and M. Hochberg, “Demonstration of a low VπL modulator with GHz bandwidth based on electro-optic polymer-clad silicon slot waveguides,” Opt. Express **18**(15), 15618–15623 (2010).
15. J. M. Brosi, C. Koos, L. C. Andreani, M. Waldow, J. Leuthold, and W. Freude, “High-speed low-voltage electro-optic modulator with a polymer-infiltrated silicon photonic crystal waveguide,” Opt. Express **16**(6), 4177–4191 (2008).
16. R. S. Jacobsen, K. N. Andersen, P. I. Borel, J. Fage-Pedersen, L. H. Frandsen, O. Hansen, M. Kristensen, A. V. Lavrinenko, G. Moulin, H. Ou, C. Peucheret, B. Zsigri, and A. Bjarklev, “Strained silicon as a new electro-optic material,” Nature **441**(7090), 199–202 (2006).
17. B. Chmielak, M. Waldow, C. Matheisen, C. Ripperda, J. Bolten, T. Wahlbrink, M. Nagel, F. Merget, and H. Kurz, “Pockels effect based fully integrated, strained silicon electro-optic modulator,” Opt. Express **19**(18), 17212–17219 (2011).
18. D. Kucharski, B. Analui, L. C. Gunn, R. Koumans, T. Pinguet, and T. Sadagopan, “Distributed amplifier optical modulator,” U.S. Patent 7 899 276 (2011).
19. J. Witzens, B. Analui, S. Mirsaidi, T. Sadagopan, B. Welch, and A. Narasimha, “Integrated control system for laser and Mach-Zehnder interferometer,” U.S. Patent 7 916 377 (2011).
20. A. Liu, L. Liao, D. Rubin, J. Basak, Y. Chetrit, H. Nguyen, R. Cohen, N. Izhaky, and M. Paniccia, “Recent development in a high-speed silicon optical modulator based on reverse-biased pn diode in a silicon waveguide,” Semicond. Sci. Technol. **23**(6), 064001 (2008).
21. J. Witzens, T. Baehr-Jones, and M. Hochberg, “Design of transmission line driven slot waveguide Mach-Zehnder interferometers and application to analog optical links,” Opt. Express **18**(16), 16902–16928 (2010).
22. D. G. Cunningham, “Traveling wave optical modulator,” U.S. Patent 5 091 981 (1992).
23. R. A. Soref and B. R. Bennett, “Electrooptical effects in silicon,” IEEE J. Quantum Electron. **23**(1), 123–129 (1987).
24. F. Vecchi, M. Repossi, W. Eyssa, P. Arcioni, and F. Svelto, “Design of Low-Loss Transmission Lines in Scaled CMOS by Accurate Electromagnetic Simulations,” J. Solid-State Circ. **44**(9), 2605–2615 (2009).

1. Introduction

Silicon Photonics (SiP) has attracted considerable attention for its potential to address the scalability issues of current short range interconnect systems. Of particular note are the fabrication of Silicon Photonics with mainstream CMOS technology [1–3] and the co-integration of electronics and optics in single chips [4]. Integrated SiP lightwave circuits have become one of the most promising technologies for next generation high data rate applications in data-centers and have recently been introduced to market by several companies [4,5]. Their compatibility with longer range communications might also make SiP a frontrunner for high-performance campus-wide networks.

Key building blocks of such interconnect systems, photodetectors [6,7] and electro-optic modulators, have been realized with group IV materials. Various technologies and architectures have been investigated in the past years in order to fabricate high-speed and low voltage electro-optic SiP modulators. From the explored actuation mechanisms for silicon based modulators, e.g. plasma modulators in both injection [8,9] and depletion mode [10–13], silicon organic hybrid (SOH) polymer modulators [14,15] and strained silicon modulators based on the Pockels effect [16,17], the depletion modulator has so far proven to be the most reliable and manufacturable approach for high-speed operation. Ring based [2] devices and Mach-Zehnder interferometers (MZI) with segmented electrodes and distributed drivers [18] each allow reduction of the radio frequency (RF) power consumption, but they also impose their own set of constraints: Resonant devices are temperature sensitive and require control systems that can be power hungry and complex to implement in the field [19], segmented electrode MZI modulators require a dense interconnection network between the electronics and the E/O modulator. While not featuring the best power consumption or drive voltage, the travelling wave electro-optic modulator remains the easiest to deploy – it is much less thermally sensitive than resonant devices and requires only a single RF port. It can also be comparatively straightforward to fabricate since it can be implemented with a single metal interconnect layer without compromising performance, as shown in the following.

#193401 - $15.00 USD Received 5 Jul 2013; revised 2 Aug 2013; accepted 3 Aug 2013; published 13 Aug 2013
(C) 2013 OSA

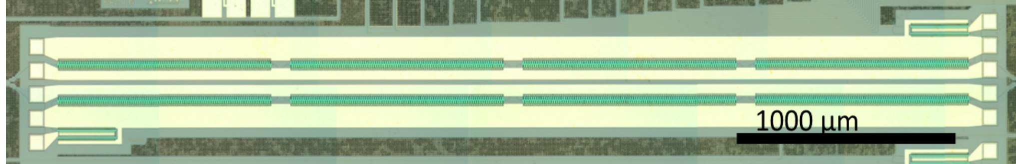

Fig. 1. Microscope image of the electro-optic modulator.

Here we focus on travelling wave carrier depletion MZI modulators. Due to the extremely short transit time in the reverse biased pn-diode, high data rates can be reached [20]. The bandwidth of the modulator reported on here is primarily limited by characteristics of the RF transmission lines, since its pn-diode RC time constant is also very high. Amongst these limitations, phase matching, RF power losses, as well as cross-talk between the signal lines in push-pull configuration [12] can play a significant role.

For this reason, the main focus of this paper is to improve the characteristics of the RF transmission lines, while maintaining an easy to fabricate, single metal layer design. We introduce two architectural improvements to the transmission lines: First, an advanced driving scheme that suppresses cross-talk between the signals applied to the two adjacent arms of an MZI driven in push-pull configuration by driving the entire modulator with a single RF mode. Second, signal line extensions that lower the resistance between the transmission line and the pn-junction inside the phase tuners while minimizing the impact on phase matching and transmission line impedance. These design improvements are experimentally validated.

In section 2 we describe a baseline device implementing the advanced driving scheme without signal line extensions. In section 3 we explain how cross-talk between signal lines is suppressed in this device. Finally, section 4 describes the signal line extensions and the additional bandwidth improvements it enables. The final device has a measured −3 dBe modulation bandwidth of 16.2 GHz (with both phase shifters DC biased at $V_d/2 = 2V$), a drive voltage $V_d = 4V$ in push-pull, 50Ω matched dual drive operation and insertion losses of IL = 8.8 dB. The final bandwidth is limited by residual phase mismatch as well as transmission line losses due to Ohmic dissipation in low doped regions inside the waveguide core that can be directly traded off with optical insertion losses and V_d. Transmission line loss models theoretically derived in [21] are experimentally verified here, making this trade-off straightforward to implement. We predict that by optimizing phase mismatch (adjusting the length of the delay lines as described in section 2) a −3 dBe O/E bandwidth in excess of 20 GHz could be reached with the same design.

2. Baseline modulator

The investigated modulators are based on a Mach-Zehnder interferometer architecture where each of the two interferometer arms consist of individual phase shifters operated in push-pull operation. The phase shifters are based on plasma dispersion in a reverse biased pn-junction embedded in a silicon waveguide. They are each driven by a ground-signal (GS) transmission line with a targeted impedance of 50Ω. The signal lines of the two arms are adjacent to each other resulting in a GSSG configuration.

Figure 1 shows a microscope image of the modulator and Fig. 2 a top view and cross-sectional schematic. The diode connectivity and driving scheme differ from a conventional push-pull architecture. One pn-diode is connected to the first signal-line S with its cathode while the other pn-diode is connected to the second signal-line S* with its anode. Thus, in order to maintain reverse biasing for both diodes, the signal-line S is only operated with positive voltages, while the signal-line S* is operated only with negative voltages relative to their associated RF ground lines. The rationale for this driving scheme will be explained in detail in section 3, "Advanced signal driving scheme".

#193401 - $15.00 USD Received 5 Jul 2013; revised 2 Aug 2013; accepted 3 Aug 2013; published 13 Aug 2013
(C) 2013 OSA

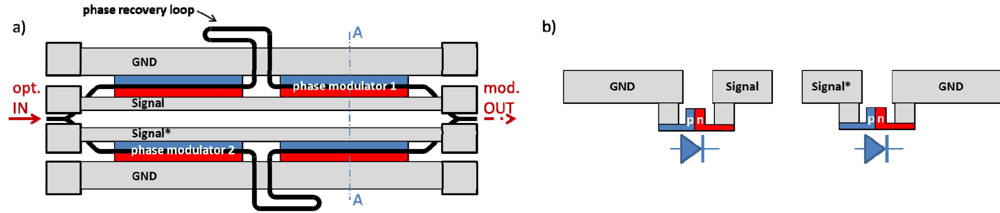

Fig. 2. Top view (a) and cross-sectional schematic (b) of the investigated modulators (not to scale).

The phase shifters each have a total length of L = 4 mm and are based on a ridge waveguide configuration. To establish phase matching between the optical mode and the RF-transmission line, recovery loops are inserted every 950 µm [12,22] as indicated in Fig. 2. These recovery loops are implemented as fully etched waveguides in order to allow for small bending radii of 10 µm. The top arm is intentionally imbalanced with an additional waveguide loop that results in a free spectral range of FSR = 5.8 nm with an extinction ratio of ER = 18dB. In addition, both arms have a low frequency phase shifter implemented in the form of a short section incorporating a forward biased pin junction allowing for precise tuning of the 3dB-operation point to the wavelength utilized in the transmitter system. The power consumption for a full π -tuning is measured to be 53 mW (36 mA at 1.46V bias).

The ridge waveguides in the phase shifter sections have a width of 400 nm and a height of 220 nm to ensure single mode operation. The slab has a thickness of 90 nm. The pn-junction is formed by a transition between nominally p^- = 3e17 cm^{-3} and n^- = 1e17 cm^{-3} doped regions (target densities) that are overlapping by 50 nm (as drawn). These doping concentrations, combined with the six transitions between high-speed phase shifters and phase recovery loops, as well as the low-speed phase tuners, result in a calculated overall insertion loss of IL_{mod} = 5.7 dB including 2.7 dB insertion loss by free carrier absorption in the doped areas of the high-speed phase tuners based on the absorption coefficients reported in [23]. The expected $V_\pi L$ (in single ended operation) is $V_\pi L$ = 2.4 V•cm and $V_{\pi/2}L$ = 1 V•cm (modeled for a 4 mm long phase shifter and renormalized to a 1 cm length, both specified here due to the non-linearity of the phase shifter transfer function) resulting in a predicted drive voltage of V_d = 2.5V. The pn-junction has a designed cutoff frequency of f_c = 36.8 GHz at 2V bias (27.3 GHz unbiased) determined by the linear capacitance C'_{WG} (F/m) and the linear series resistance R'_{WG} (Ω•m) of the pn-junction, the latter resulting from the low-doped silicon waveguide and the highly-doped slab that electrically connect the pn-junction to the metal signal and ground lines (Fig. 2(b)). The linear capacitance and the linear resistance of the diode were targeted to be R'_{WG} = 18.8 mΩ•m and C'_{WG} = 230 pF/m at 2V DC bias (310 pF/m unbiased) assuming an abrupt p/n junction. Due to overlapping p^- and n^- doped regions and slightly higher doping concentrations than initially targeted, the linear capacitance and resistance values had to be adjusted based on experimental data in the following analysis.

To validate the low-speed design characteristics and compare them to the fabricated device, we have measured the static voltage dependent optical transmission spectrum to determine $V_\pi L$ and IL. Figure 3 shows the phase shift respectively introduced in the top and bottom arms as a function of the applied bias voltage. The phase shift is extracted from the wavelength shift of the optical transmission spectrum at different static modulation voltages displayed in the inset. From this we can derive a $V_\pi L$ = 4.0 V•cm and $V_{\pi/2}L$ = 1.6 V•cm for single ended operation resulting in a drive drive voltage V_d = 4V in dual drive configuration. The de-embedded insertion losses of the modulator, after normalizing out coupling losses from the grating couplers used to couple light to and from the chip, are IL = 8.8 dBm.

In addition, we have conducted High-Frequency-Capacitance-Voltage (HFCV) measurements at a frequency of f_{AC} = 1 MHz and a modulation amplitude of V_{AC} = 100 mV on each phase shifter loaded transmission line. The measured value for the loaded transmission line without pre-biasing is C'_{TL+WG} = 600 pF/m. This results in an extracted junction

#193401 - $15.00 USD Received 5 Jul 2013; revised 2 Aug 2013; accepted 3 Aug 2013; published 13 Aug 2013
(C) 2013 OSA

capacitance of C'_{WG} = 360 pF/m at 0V biasing and C'_{WG} = 250 pF/m at $V_d/2$ = 2V. From RF-measurements (Fig. 8) we derive a series resistance of R'_{WG} = 13.9 mΩ•m.

The lower resistance is partially accounted for by a measured increase of the n- and p-doped sheet resistances attributed to a 30% higher doping level in the low-doped regions inside the waveguide as compared to target. The lower capacitance observed in experiment is consistent with the higher measured V_d. Both can be reproduced in simulations by assuming a reduced doping region between n- and p- where these two implants overlap. The higher insertion losses are partially attributed to excess losses in the Y-junctions as well as to the higher implant densities (calculated as an additional 0.7 dB). The experimentally determined capacitance and resistance values are assumed in the rest of the paper and result in a diode frequency cutoff of 45.8 GHz at 2V reverse bias (31.8 GHz unbiased). In order to confirm the diode frequency cutoff we have measured ring resonator based modulators that have a phase shifter with the same pn junction configuration. The electro-optical transmission measurements show a cutoff frequency above 40 GHz limited by the bandwidth of our measurement setup. Since these frequencies by far exceed the measured MZI-modulator bandwidth, we can safely conclude that transmission line losses, phase mismatch and cross-talk are the limiting factors of the observed modulator bandwidth – the latter being taken care of by design as explained in section 3.

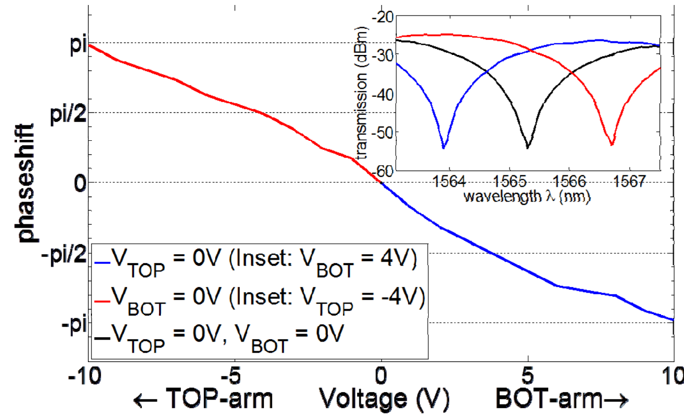

Fig. 3. Phase shifts induced in the top (red curve) and bottom (blue curve) MZI arms as a function of applied voltages. The inset shows exemplary transmission spectra for several applied voltages (see legend).

At low frequencies, the transmission line losses are dominated by Ohmic losses in the metal lines, with losses scaling with the well-known dependency as $dB/\left(cm\cdot\sqrt{Hz}\right)$. However, at higher frequencies the transmission line losses are determined by the Ohmic losses arising from the series resistance of the pn-diode inside the silicon slab and the silicon waveguide. The excess RF losses below the diode cutoff were derived in [21] as

$$\alpha(f)=\alpha_0\sqrt{f}+R'_{WG}(2\pi\cdot f\cdot C'_{WG})^2\cdot Z_{TL}=\alpha_0\sqrt{f}+\alpha_1 f^2, \tag{1}$$

with α_0 the scaling factor for the baseline losses of the transmission line, α_1 the scaling factor for the Ohmic losses inside the silicon and Z_{TL} the impedance of the loaded transmission line. Since in a reverse biased pn-junction based phase modulator the capacitance of the junction C'_{WG} is dependent on the applied modulation voltage, the excess losses are voltage dependent. However, in the small-signal regime corresponding to the VNA measurements the junction capacitance can be considered to be constant. Moreover, the voltage dependence of the diode capacitance of our device is rather small in the range of operation as shown by the almost linear voltage dependent phase shifts displayed in Fig. 3.

#193401 - $15.00 USD Received 5 Jul 2013; revised 2 Aug 2013; accepted 3 Aug 2013; published 13 Aug 2013
(C) 2013 OSA

Equation (1) was verified experimentally by measuring the frequency dependent transmission line losses of the modulator. These results are reported in section 4.

We define the effective length of the modulator as:

$$L_{eff} = \int_0^L e^{-\alpha/2\cdot x} dx \qquad (2)$$

Assuming perfect phase matching as well as a linearized phase shift versus applied voltage (which is correct in the small signal limit applied by the vector network analyzer) this corresponds to the length of a modulator with ideal, lossless transmission lines that would result in the same optical signal amplitude. We report the electro-optical S-parameters in dBe (electrical RF-power at the output of the photodiode corrected for photodiode bandwidth). The bandwidth of an electro-optic modulator can be reported either with the optical convention at −6 dBe, where the optical modulation amplitude (OMA) is reduced by 50%, i.e., $20\cdot\log_{10}(\mathrm{OMA}) = -6\,\mathrm{dBe}$ and $L_{eff} = L/2$, or with the more conservative and more widely used electrical convention at −3 dBe where the electrical RF-power at the photoreceiver output has decreased by 50%, i.e., $20\cdot\log_{10}(\mathrm{OMA}) = -3\,\mathrm{dBe}$ and $L_{eff} = L/\sqrt{2}$. In this paper we report both metrics for completeness.

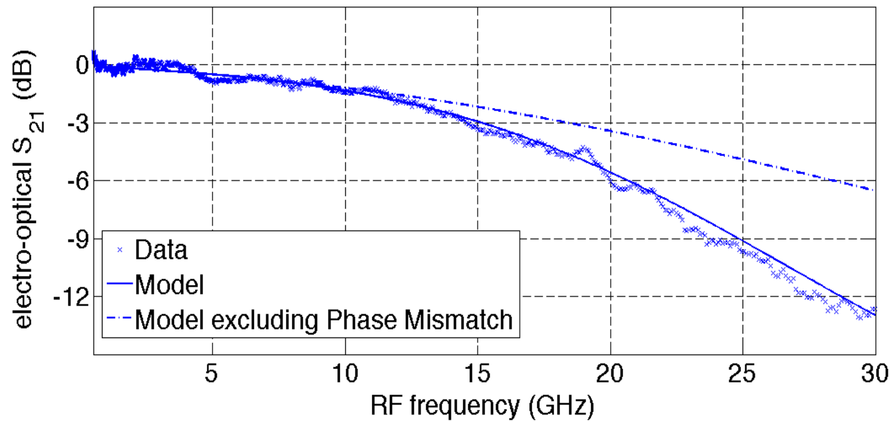

Fig. 4. Electro-optical transmission coefficient S_{21} as a function of the RF-frequency. The experimental data is compared to models calibrated with experimental data taking into account transmission line losses and phase mismatch.

Figure 4 shows the normalized electro-optical transmission coefficient S_{21} as a function of the RF-frequency for the baseline device (without electrode extensions) at a bias-voltage of $V_d/2$ = 2V and compares it to analytical models respectively taking into account transmission line losses only (Eqs. (1) and (2)) or transmission line losses and phase mismatch as extracted from the experimental data in sections 3 and 4. The raw data crosses the −3 dBe and −6 dBe lines at respectively f_{-3dB} = 14.53 GHz and f_{-6dB} = 20.03 GHz. The modeled values are f_{-3dB} = 15.03 GHz and f_{-6dB} = 20.61 GHz. In the absence of phase mismatch this modulator would have reached f_{-3dB} = 18.17 GHz and f_{-6dB} = 28.41 GHz. The transmission line indices assumed in the fit in Fig. 4 correspond to n_{RF} = 4.1 at 10 GHz (consistent with the RF-TDR measurements in section 4), as well as 3.6 and 3.35 at respectively 20 GHz and 30 GHz as extracted from a calibrated HFSS model. The values for the fitting parameters α_0 and α_1 have been extracted from electrical transmission line loss measurements as described in section 4.

Since the effective index of a transmission line loaded with a depletion type phase shifter is frequency dependent [21], perfect phase matching can be challenging to reach for a broad frequency range, but can be obtained at least for a target frequency. In our modulator, the

#193401 - $15.00 USD Received 5 Jul 2013; revised 2 Aug 2013; accepted 3 Aug 2013; published 13 Aug 2013
(C) 2013 OSA

phase mismatch is primarily due to a suboptimal delay loop length and could thus easily be improved. We have verified with modeling that optimizing the delay loops for 20 GHz operation would have very little impact at lower frequencies in this specific design, due to the lower sensitivity on phase mismatch at lower frequencies.

Applying a DC-bias voltage to both arms symmetrically enlarges the depletion width and thereby decreases the capacitance of the pn-junctions. Thus, the optical modulation bandwidth is increased. However, the increased modulation bandwidth is then traded off against reduced optical modulation amplitude. A bias of $V_d/2$ corresponds to a realistic system environment and is thus used as the standard for all the measurements in this paper.

As can be seen in Fig. 1, the signal lines are located extremely close to each other. As shown in section 3, this transmission line geometry could lead to severe cross-talk for a different driving scheme. We will also explain how this cross-talk was suppressed in our device. In section 4 we will show how signal line extensions can serve to further improve the modulator bandwidth without changing its transmission lines' impedance or phase velocity.

3. Advanced signal driving scheme

The first diode connectivity that may come to mind for a depletion type MZI-modulator driven in push-pull configuration may be to connect the cathode of both diodes to positively driven signal lines, since the cathodes need to remain at positive voltages. In this case, the two arms of the interferometer receive complementary data-signals, i.e., if one arm receives a voltage associated with a logical '1' the other arm receives a voltage associated with the complementary logical '0', and vice-versa as illustrated in Fig. 5(a). Thus, this driving scheme necessitates both the data signal *'S'* as well as the complementary data signal '$\overline{S}$'. Since S and $\overline{S}$ are different signals from an RF point of view – they are actually exactly opposite – cross-talk between the signal lines can become an issue unless a significant separation is allowed for in between the two SG transmission lines or shielding is implemented with a multi-layer back-end process. Since cross-talk is frequency dependent, this directly impacts the bandwidth of the modulator.

Let us consider for example the case of a $GS\overline{S}G$ configuration where a signal S is applied to the first signal line and the inverted signal $\overline{S}$ is applied to the second signal line. When applying data, we will excite three super-modes of the coupled transmission lines: one symmetric mode and two anti-symmetric modes (Figs. 6(c)-6(e)), with symmetries defined by the voltage distribution (note that Fig. 6 shows the E-fields that have opposite symmetry). Each mode has a different propagation constant β_{sym}, β_{asym1} and β_{asym2}. While the symmetric mode and the first anti-symmetric mode both apply a significant voltage across the two phase shifters, the difference consists primarily in whether the same or opposite RF voltages are applied to the two pn-junctions, the second anti-symmetric mode is very different: It results in a very small RF voltage applied across the pn-diodes, with most of the voltage dropped across the two (inner) signal lines. For this reason, the second anti-symmetric mode is almost completely insensitive to the excess capacitance of the pn-junctions and has thus a much higher phase velocity [21]. The beating between these three RF modes gives rise to significant cross-talk in the frequency range of interest (Figs. 6(a)-6(b)).

#193401 - $15.00 USD Received 5 Jul 2013; revised 2 Aug 2013; accepted 3 Aug 2013; published 13 Aug 2013
(C) 2013 OSA

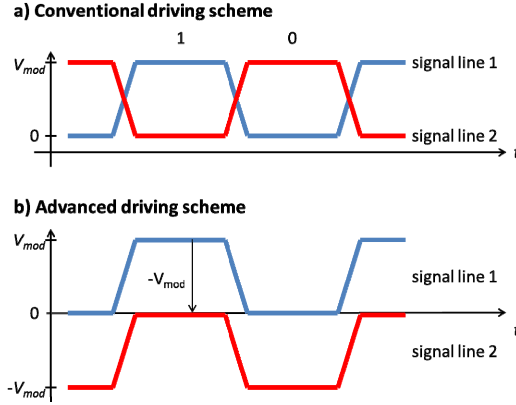

Fig. 5. Signals for (a) the conventional and (b) the advanced driving scheme.

To model the cross-talk between the signal lines for the conventional signal driving scheme we have calculated the voltages V and currents I for each of the four metal lines for the three modes using a 2D finite elements mode solver (Ansoft HFSS, f = 18 GHz):

$$V_{sym} = \begin{bmatrix} 0 \\ 5.26 \\ 5.26 \\ 0 \end{bmatrix}, \qquad I_{sym} = \begin{bmatrix} -0.096 \\ 0.096 \\ 0.096 \\ -0.096 \end{bmatrix}$$
$$V_{asym1} = \begin{bmatrix} 2.89 \\ -1.59 \\ 1.59 \\ -2.89 \end{bmatrix}, \quad I_{asym1} = \begin{bmatrix} 0.109 \\ -0.112 \\ 0.112 \\ -0.109 \end{bmatrix}, \tag{3}$$
$$V_{asym2} = \begin{bmatrix} -3.72 \\ -3.59 \\ 3.59 \\ 3.72 \end{bmatrix}, \quad I_{asym2} = \begin{bmatrix} -0.058 \\ -0.079 \\ 0.079 \\ 0.058 \end{bmatrix}$$

where the voltages are given in V and the currents in A, and where the normalization is chosen as unit power (1W). The symmetric mode is close to the target 50Ω impedance (55Ω).

To solve for the voltages and currents at the end of the transmission line we apply a self-consistent scattering matrix analysis taking into account multiple reflections from the beginning and the end of the transmission line arising from the impedance mismatch between the individual super-modes and the 50Ω RF-probe-tips. As boundary conditions, we assume 50Ω terminations on either end of the signal lines and take into account shorting of the two ground lines inside the probe tips. The frequency dependent losses of the RF modes were directly taken from simulations. The effective indices of the loaded symmetric and anti-symmetric RF modes (n_{sym} and n_{asym1}) were rescaled to 80% of their simulated value in order to match the experimentally determined phase velocity for the symmetric mode (as determined by time domain reflectometry, see Fig. 9). The same rescaling factor was used to predict the transmission line velocities used for the models fitting the responses of the baseline and enhanced modulators (Figs. 4 and 10).

#193401 - $15.00 USD Received 5 Jul 2013; revised 2 Aug 2013; accepted 3 Aug 2013; published 13 Aug 2013
(C) 2013 OSA

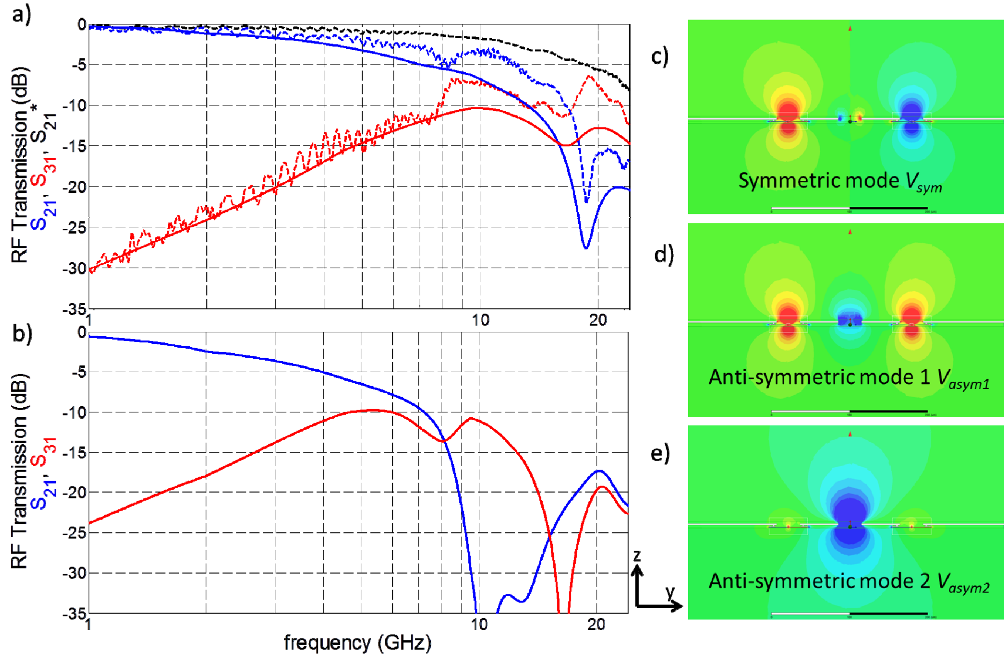

Fig. 6. (a) Transmission coefficients $S_{21,RF}$ (blue trace, transmission through signal line 1) and $S_{31,RF}$ (red trace, cross-talk to signal line 2) measured at the end of the transmission line for an RF signal applied only to signal line 1, corresponding to the cross-talk occurring in the conventional driving scheme. Dashed curves are measured and continuous curves are modeled. The black curve shows the measured transmission coefficient $S_{21,RF}$* of the symmetric mode, for comparison, corresponding to RF losses in the advanced driving signal scheme. (b) Modeled $S_{21,RF}$ and $S_{31,RF}$ for an MZI modulator with a doubled, 8 mm length. Here too, the blue line is the RF transmission and the red line shows the cross-talk. (c-e) Super-modes supported by the GSSG-transmission line (E_y). The symmetric mode has an anti-symmetric E_y field, but symmetric voltages.

Figure 6(a) shows the measured transmission coefficients $S_{21,\mathrm{RF}}$ and $S_{31,\mathrm{RF}}$ recorded at the ends of the two signal lines when only one of the signal lines is driven with an RF signal at the input while the other is 50Ω terminated at both its input and output, i.e. RF signal amplitudes V_{in} = [0, 1, 0, 0]. This corresponds to the cross-talk encountered in the conventional driving scheme with complementary signals S and $\overline{S}$. $S_{21,\mathrm{RF}}$ is the transmission through the driven signal line while $S_{31,\mathrm{RF}}$ is the cross-talk. The continuous curves show the theoretical transmission coefficients based on the modal analysis. In addition, we plotted the measured transmission coefficient S_{21}* for a symmetrically driven input (dashed black curve), i.e., RF drive voltage amplitudes V_{in}* = [0, 1, 1, 0], in order to show the RF-attenuation of the symmetric mode. This corresponds to the RF losses in the advanced driving scheme described below. It is apparent that cross-talk becomes an issue at much lower frequencies than the RF transmission line losses.

From the quality of the fit shown in Fig. 6(a) we can conclude that the beating between the three super-modes adequately models the experimentally measured cross-talk. The magnitude of the cross-talk is matched very well below 10 GHz. At higher frequencies the salient features of the experimental data are also qualitatively reflected by the model. It is important to note that the first cross-talk features appear at 8 GHz, while the bandwidth of our single-RF-mode modulator is substantially higher, validating the importance of suppressing cross-talk. As expected, cross-talk becomes even more drastic for longer modulators. To exemplify this we are showing the modeled cross-talk for an 8 mm long modulator in Fig. 6(b). It can be seen that cross-talk becomes severe above a few GHz, very severely limiting the bandwidth of the modulator.

Now, when the modulator is driven in a conventional $GS\overline{S}G$ configuration the following voltages are applied to the four metal lines for the two different bit-states (the voltages are normalized to the modulation voltage V_{mod}):

$$\vec{V}_{in,0} = \begin{bmatrix} 0 \\ 1 \\ 0 \\ 0 \end{bmatrix} = \begin{bmatrix} 0 \\ 1/2 \\ -1/2 \\ 0 \end{bmatrix}_{AC} + \begin{bmatrix} 0 \\ 1/2 \\ 1/2 \\ 0 \end{bmatrix}_{DC},$$
$$\vec{V}_{in,1} = \begin{bmatrix} 0 \\ 0 \\ 1 \\ 0 \end{bmatrix} = \begin{bmatrix} 0 \\ -1/2 \\ 1/2 \\ 0 \end{bmatrix}_{AC} + \begin{bmatrix} 0 \\ 1/2 \\ 1/2 \\ 0 \end{bmatrix}_{DC} \tag{4}$$

with the voltage vector $\vec{V}_{in,0}$ corresponding to the 0-bit and $\vec{V}_{in,1}$ corresponding to the 1 bit. The vectors can be decomposed into a part that is not dependent on the bit-state and represents the phase shifter bias-voltages necessary to maintain the pn-junctions in reverse bias (denoted as DC) and a voltage vector that is dependent on the bit-state and oscillates at the rate of the applied RF-field (denoted as AC). The AC component can be decomposed into a superposition of super-modes described by Eq. (3). The differing RF wave propagation numbers are resulting in cross-talk and thus a reduced analog bandwidth, as previously discussed.

In order to overcome this limitation, we investigated a driving scheme that relies on a single RF super-mode inside the coupled transmission lines. We now assume the diode connectivity to be given by the diagram in Fig. 2(b), i.e., one diode has its cathode connected to a signal line *S* while the other diode has its anode connected to a signal line *S**. Again, we assume push-pull operation, i.e, the two phase shifters apply opposite phase shifts. In order to maintain both diodes in reverse operation, the input voltages applied to the four GSS*G lines are given by

$$\vec{V}_{in,0} = \begin{bmatrix} 0 \\ 1 \\ 0 \\ 0 \end{bmatrix} = \begin{bmatrix} 0 \\ 1/2 \\ 1/2 \\ 0 \end{bmatrix}_{AC} + \begin{bmatrix} 0 \\ 1/2 \\ -1/2 \\ 0 \end{bmatrix}_{DC}$$
$$\vec{V}_{in,1} = \begin{bmatrix} 0 \\ 0 \\ -1 \\ 0 \end{bmatrix} = \begin{bmatrix} 0 \\ -1/2 \\ -1/2 \\ 0 \end{bmatrix}_{AC} + \begin{bmatrix} 0 \\ 1/2 \\ -1/2 \\ 0 \end{bmatrix}_{DC}, \tag{5}$$

where again $\vec{V}_{in,0}$ and $\vec{V}_{in,1}$ are the input voltages for a logical zero and a logical 1. In the decomposition on the right side of the equations it is apparent that the time-varying term corresponds to the symmetric super-mode of the coupled transmission line system, only. Since it is the only RF mode being excited, there is obviously no cross-talk.

In addition to the eliminated cross-talk and to the associated bandwidth improvement, this configuration also allows for a simpler driver architecture. For conventional driving schemes with complementary signals, two data streams are needed. On the other hand, for the advanced single-RF-mode driving scheme investigated here the voltages on signal lines 1 and 2 are just offset by a constant voltage and are not inverted. If *S* varies between 0 and V_{mod}, *S** is simply S-V_{mod} and can be generated from *S* with a bias-T. Thus, the generation of a

complementary data stream is not necessary here. Figure 5 illustrates the different signals applied to signal lines 1 and 2 (blue and red curves, respectively) for the conventional driving scheme and the advanced driving scheme.

In order to measure the devices in this configuration, we fed the output of the vector network analyzer to a 3 dB splitter. After DC-shifting the outputs of the splitter with bias-Ts, the two resulting signals were fed into the coupled transmission lines via a GSSG probe tip.

For an integrated driver plus modulator solution, the on-chip implementation of a 3 dB splitter or a bias-T might consume a substantial amount of chip area. However, a second driving scheme can be implemented that is equivalent from an RF point of view, but does not require either one of these devices. The states for the 0- and 1-bits are then chosen as

$$\begin{aligned} \vec{V}_{in,0} &= \begin{bmatrix} 0 \\ 1 \\ 1 \\ 1 \end{bmatrix} = \begin{bmatrix} 0 \\ 1/2 \\ 1/2 \\ 0 \end{bmatrix}_{AC} + \begin{bmatrix} 0 \\ 1/2 \\ 1/2 \\ 1 \end{bmatrix}_{DC} \\ \vec{V}_{in,1} &= \begin{bmatrix} 0 \\ 0 \\ 0 \\ 1 \end{bmatrix} = \begin{bmatrix} 0 \\ -1/2 \\ -1/2 \\ 0 \end{bmatrix}_{AC} + \begin{bmatrix} 0 \\ 1/2 \\ 1/2 \\ 1 \end{bmatrix}_{DC} \end{aligned} \tag{6}$$

These signals can be generated by shorting S and S^* and simply setting the second RF-ground (the fourth line) to the constant voltage + V_{mod}. In this case the two signal lines can also be reduced to a single line within the modulator, further shrinking the device size.

4. Advanced pn-junction contacting scheme

The second limiting factor for the modulator bandwidth comes from the signal attenuation in the transmission lines. Especially at higher frequencies this is dominated by the Ohmic losses in the doped silicon regions (R'_{WG}) that carry the current between the pn-junction located in the waveguide (C'_{WG}) and the metal lines. The corresponding RF losses and their effect on the optical modulation amplitude are described by Eqs. (1) and (2). Note that the impedance of the transmission lines is a primary driver of their RF-losses and thus of the modulator bandwidth. A lower impedance results in lower RF-losses as shown by Eq. (1), but it also results in a higher power consumption. The silicon doping levels usually result out of a trade-off between high enough doping to provide low RF losses and thus a high bandwidth and low enough doping to provide low optical attenuation and thus low optical insertion losses. In order to partially deconstrain this problem, two different implants are typically utilized (Fig. 7(a)): one relatively low dose implantation that overlaps with the optical mode ($R'_1 + R'_2$) and a high dose implantation outside the optical mode to reduce the series resistance ($R'_3 + R'_4$).

An intuitive way to decrease the resistances R'_3 and R'_4 would be to reduce the distance between the waveguide and the metal lines, since this would also reduce the length of silicon the current has to flow through in order to reach the pn-junction. However, in a single metal interconnect configuration this distance is also fixed by the impedance of the transmission line Z_{TL} one wishes to obtain. Z_{TL} is determined by the linear capacitance C'_{TL+WG} (including both the intrinsic capacitance of the unloaded transmission line and the capacitance of the pn-junction) and the linear inductance L'_{TL} ($Z_{TL} = \sqrt{L'_{TL} / C'_{TL+WG}}$). Since the conductivity of the doped silicon typically remains a few orders of magnitude below the conductivity of the metal, the longitudinal currents flowing in the transmission line are primarily confined to the metal lines. Under these conditions, both L_{TL} and C_{TL} are simply determined by the distance between the ground and signal line [21].

#193401 - $15.00 USD Received 5 Jul 2013; revised 2 Aug 2013; accepted 3 Aug 2013; published 13 Aug 2013
(C) 2013 OSA

In order to compensate for the high capacitive load of the pn-junction, the linear inductance of the transmission line has to be increased, e.g., by increasing the distance between the signal line and the ground line. However, this also increases the resistances R'_3 and R'_4 and thereby increases the RF attenuation. In our baseline modulator, based on simulations, the resistances R'_3 and R'_4 make up for 42% of the total diode series resistance $R'_{WG} = R'_1 + R'_2 + R'_3 + R'_4$, thus significantly affecting the transmission line losses. In order to recover as much as possible of this penalty, we introduce a contacting scheme based on individual metal extensions transversely connecting the metal lines to the waveguide (approximating an artificial material with anisotropic conductivity). Figure 7(b) shows the unit cell of the transmission line with electrode extensions.

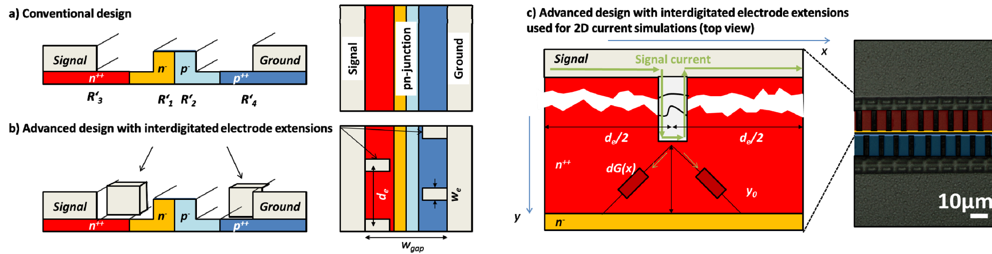

Fig. 7. (a) conventional design of a loaded transmission line, (b) advanced design with interleaved electrode extensions (c) lumped element representation of the current flow. The microscope image shows a detail of the electrode extensions in the real modulator. The dark boxes are the metal electrode extensions; the colored areas represent the different doping regions. Grey areas are signal and ground line, respectively.

Due to the sparsity of the metal extensions, the induced excess capacitance is very small. Moreover, the current flowing through the extensions is restricted to a transverse current flowing to and from the pn-junction and remains much smaller than the longitudinal current flowing along the metal lines. Thus, the excess inductance created by the metal extensions is also small. In order for the assumption of a primarily transverse current in the electrode extensions to hold, the extensions need to have sufficient spacing between each other in the longitudinal direction to prevent longitudinal current flow via capacitive coupling. Furthermore, the extensions from the signal and ground lines are interleaved relative to each other, to minimize the additional capacitance created by them. The concept can be seen in analogy to the ground plane engineering reported in [24], where a ground plane was slotted to prevent longitudinal currents and thus modify the impedance of an RF strip line. While the impact on the impedance of the transmission line is minimized, the series resistance of the pn-diode is significantly reduced.

In the advanced modulator investigated here, metal electrode extensions were implemented with a width of $w_e = 2\mu m$ and with an extension-to-extension separation (along the metal line) of $d_e = 10\mu m$. They are reaching as close to the pn-junction as possible without perturbing the optical mode propagating in the waveguide. Due to the much lower resistance of the metal extensions, the majority of the depletion current that flows to and from the pn-junction will flow through them, thus significantly shortening the distance over which it flows through the doped silicon slab.

Since the extension-to-extension spacing is significantly smaller than the distance of the waveguide to the metal lines ($w_{gap}/2$ = 15 µm, where w_{gap} is the distance between the two signal lines), the resistance corresponding to transport through the silicon slab region is significantly reduced. A 2D-simulation of the current flow shows a reduction of the total series resistance by 37%, which means that close to 90% of the resistances R'_3 and R'_4 has been removed by introducing the metal electrode extensions.

As already explained, the effect of the electrode extensions on the linear capacitance C'_{TL} and linear inductance L'_{TL}, and thus on the transmission line impedance and phase velocity, is expected to be very small. This was verified by simulating the unit cell with a 3D simulation in HFSS. In particular, this corresponds to a situation where currents in the metal extensions

#193401 - $15.00 USD Received 5 Jul 2013; revised 2 Aug 2013; accepted 3 Aug 2013; published 13 Aug 2013
(C) 2013 OSA

primarily flow transverse to the direction of the transmission line. The vanishing effect of the metal extensions on transmission line impedance, transmission line phase velocity and waveguide losses was also experimentally validated as described in the following.

Optical transmission measurements averaged over 6 different dies showed a slight *reduction* in insertion losses of 0.3 dB which is well within the statistical uncertainty of the measurements and thus attributed to measurement error. Thus, we conclude that the electrode extensions do not have a significant influence on the optical mode and do not add optical losses.

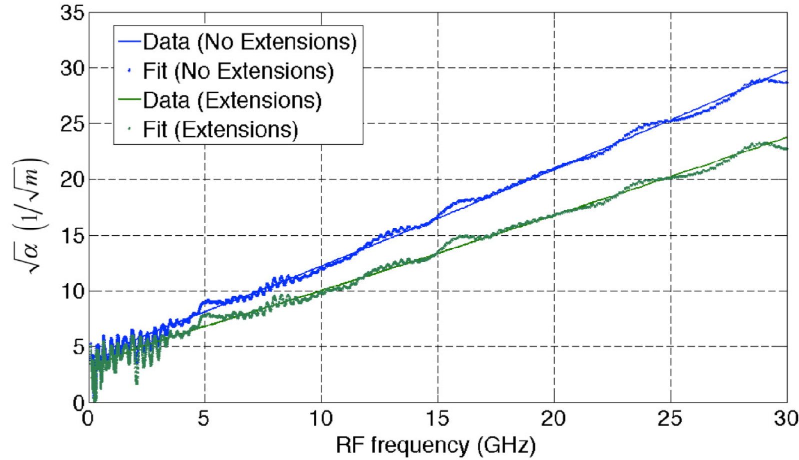

Fig. 8. Transmission line attenuation for the modulator with and without electrode extensions. The y-axis corresponds to $\sqrt{\alpha}$ rather than α in order to make the trend predicted by Eq. (1) apparent by a linear progression. Continuous lines are fitted according to Eq. (1).

Figure 8 shows the measured transmission line attenuation α as a function of RF-frequency. We display the square root of the attenuation coefficient to verify the trend predicted by Eq. (1). In the high frequency regime, above a few GHz, the losses are dominated by the second term of Eq. (1) corresponding to Ohmic losses in the series resistance of the pn-diode. These correspond to a constant slope on the graph. The solid lines show a fit of the measured data using Eq. (1). The two fitted curves coincide very well with the measured data. As fitting coefficients we extracted α_0 = 5.56e-4 $m^{-1}Hz^{-1/2}$ and α_1 = 0.91e-18 $m^{-1}Hz^{-2}$ for the modulator without electrode extensions and α_0 = 4.31e-4 $m^{-1}Hz^{-1/2}$ and α_1 = 0.56e-18 $m^{-1}Hz^{-2}$ for the modulator with electrode extensions. It is apparent that at high frequencies the losses of the transmission line with the electrode extensions are lower by 38% relative to the baseline modulator. Since the high frequency losses are directly proportional to the series resistance of the pn-junction, we can also confirm a reduction of the series resistance by 38%, very close to the 37% predicted by simulation. It should also be noted that the curves in Fig. 8 stay straight at high frequencies up to the upper limit of the measurement range. This confirms that the diode cutoff lies at a higher frequency, since the linear progression would slow down beyond the diode cutoff frequency, resulting in an inflection point [21].

In order to further experimentally validate the design, especially to validate that the impedance and phase velocity of the transmission lines are not significantly modified, we measured the reflection S_{11} of the combined GSSG-signal lines in the time domain (time domain reflectrometry – TDR, see Fig. 9). Discontinuities in the impedance of a transmission line cause a measurable increase in the reflection coefficient. The magnitude of the reflection coefficient is thus a measure of the impedance mismatch that causes the reflection. The temporal distance between two reflections can be translated into a signal velocity or an

#193401 - $15.00 USD Received 5 Jul 2013; revised 2 Aug 2013; accepted 3 Aug 2013; published 13 Aug 2013
(C) 2013 OSA

effective dielectric constant when correlated with a spatial distance. To identify the beginning of the transmission line, we measured the reflection coefficient with the probe tip lifted up from the chip to get a strong reflection from the open end of the probe tip. Next, we landed the probe tip on the input pads of the modulator transmission line leaving the output pads unterminated. This reduces the reflection from the input of the transmission line due to the better impedance match while at the same time also gives a second strong reflection from the unterminated output pads.

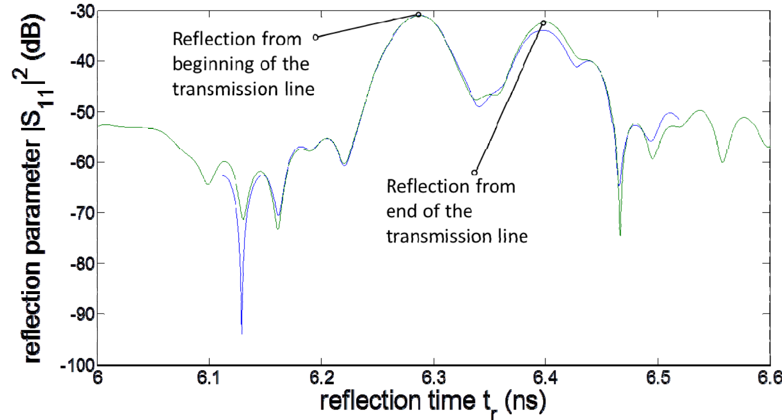

Fig. 9. TDR measurement of S_{11} for conventional (blue curve) and advanced transmission line design with electrode extensions (green curve).

Thus, the phase velocity of the RF signal can be directly measured according to the time delay between the two peaks. By this method we have measured n_{RF} = 4.125 for both devices with and without electrode extensions. This indicates that the introduction of the electrode extensions does not add an additional phase mismatch between the RF-driving signal and the optical wave. In addition, the reflections from the input of the transmission lines have the same magnitude in both cases. This is a strong indication that both transmission lines have almost identical impedances. Therefore, we can conclude that the introduction of the interleaved electrode extensions did not have a significant impact on the impedance matching and phase matching of the modulator.

Table 1. Comparison of measured and modeled bandwidths for the modulator with and without electrode extensions

-3 dBe	**Data**	**Predicted (including phase mismatch)**	**Predicted (without phase mismatch)**
Without Extensions	14.53 GHz	15.03 GHz	18.17 GHz
With Extensions	16.19 GHz	16.78 GHz	23.2 GHz
-6 dBe	**Data**	**Predicted (including phase mismatch)**	**Predicted (without phase mismatch)**
Without Extensions	20.03 GHz	20.61 GHz	28.41 GHz
With Extensions	22.56 GHz	22.12 GHz	35.7 GHz

Figure 10 shows the electro-optical transmission coefficients S_{21} of the baseline modulator without electrode extensions (blue curve, same as in Fig. 4) and a modulator with the interleaved electrode extensions. The solid lines again show a fit assuming transmission line losses with a frequency dependence given by Eq. (1) and coefficients extracted from Fig. 8, as well as a frequency dependent transmission line index extracted from a calibrated HFSS simulation (same as for the model in Fig. 4). It can be seen that both modulators are modeled extremely well. The measured and modelled frequency roll-off characteristics of the modulators with and without electrode extensions are summarized in Table 1.

#193401 - $15.00 USD Received 5 Jul 2013; revised 2 Aug 2013; accepted 3 Aug 2013; published 13 Aug 2013
(C) 2013 OSA

Since in the absence of phase mismatch the f_{-3dB} and f_{-6dB} bandwidths scale as the inverse square root of the diode series resistance (Eqs. (1) and (2)), one would expect the modulator bandwidth to be improved by 26% after introduction of the electrode extensions. Measured at 11%, the actual improvement is however significantly lower. This is adequately modelled once phase mismatch is taken into account (both modulators suffer from identical phase mismatch that is independent from the electrode extensions). Since in the presence of phase mismatch later portions of the modulator are less efficient or even work against the already accumulated phase shift, transmission line losses introduce a reduced penalty and the effect of reducing the diode series resistance is thus lower. It is however expected that a higher improvement would have been obtained in a better phase matched device, as can be read from the last column of Table 1.

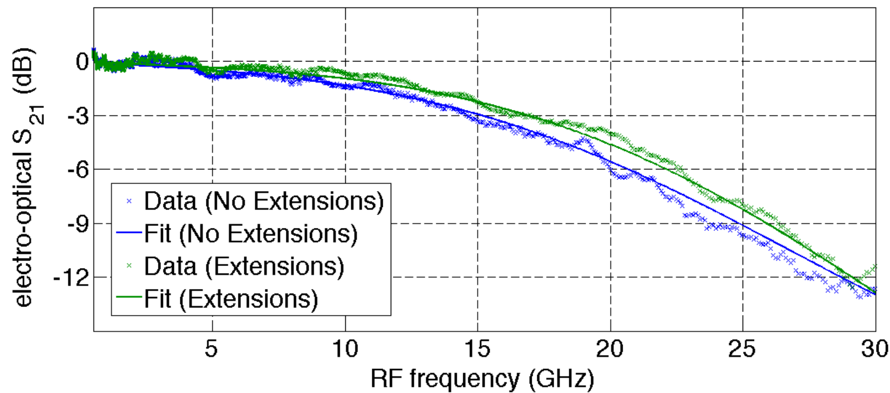

Fig. 10. Optical transmission coefficient S_{21} of the conventional baseline modulator (blue) and a modulator with an advanced transmission line design with interleaved electrode extensions (green). Solid lines are models based on experimentally extracted parameters.

5. Conclusion

We have investigated two novel concepts for the transmission line design for travelling wave Mach-Zehnder interferometer based Silicon Photonics modulators that have a significant impact on the optical modulation bandwidth of the devices.

We have been able to show that using an advanced signal driving scheme, the cross-talk between the signal lines of a push-pull modulator could effectively be suppressed and thus the corresponding bandwidth limitation overcome. Furthermore, bandwidth limitation resulting from transmission line losses associated to the series resistance of the pn-diode have been adequately modeled and reduced by the introduction of slotted electrode extensions.

Acknowledgments

The authors would like to acknowledge support by the European Research Council (ERC) under the project “Frontiers of Integrated Silicon Nanophotonics in Telecommunications” (ERC FP7/2011-2016 No. 279770), by the European Union’s Seventh Framework Programme (CIG FP7/2011-2015 No. 293767) and by the German Ministry for Research and Education (BMBF) under the CELTIC + project “Safe and Secure European Router” (SASER, contract No. 16BP12504). The devices were fabricated via the shuttle service OpSIS at Singapore’s Institute of Microelectronics (IME).